Journal of Materials Chemistry A

ROYAL SOCIETY OF CHEMISTRY

PAPER

View Article Online
View Journal | View Issue

Cite this: J. Mater. Chem. A, 2024, 12, 30522

A soft molecular single-source precursor approach to synthesize a nanostructured Co_9S_8 (pre)catalyst for efficient water oxidation and biomass valorization†

Basundhara Dasgupta, [a] Suptish Ghosh, [a] Carsten Walter,[b] Markus S. Budde,[a] Georg J. Marquardt,[a] Han-Hsu Chen,[a] Markus G. M. Breithaupt,[a] Tolga Yilmaz,[a] Christoph Garmatter, [a] Tamanna Ahamad, [c] Ingo Zebger, [c] Matthias Driess [a] and Prashanth W. Menezes *[ab]

The molecular single-source precursor (SSP) route has emerged as a promising avenue for synthesizing highly efficient electro(pre)catalysts tailored for both oxygen evolution (OER) and organic electrooxidation reactions. This study introduces a novel $[Co^{II}(PyHS)_4(OTf)_2]$ molecular complex, offering a facile route to access the nanocrystalline Co_9S_8 phase. Upon application in alkaline OER, Co_9S_8 displayed remarkably high electrocatalytic activity across various metrics, including overpotentials, Tafel slopes, faradaic efficiency, charge transfer resistance, turnover frequency, electrochemical surface area, Co-redox active sites, and long-term stability at industrially relevant current densities (for 80 h at 100 mA cm^{-2}) outperforming its Co-based counterparts under identical conditions. In-depth analysis employing several *ex situ* techniques revealed the complete leaching of sulfur and irreversible reconstruction of Co_9S_8 into a cobalt oxyhydroxide active phase during the OER. Moreover, quasi *in situ* Raman spectroscopy provided insights into the presence of $Co^{IV}O_2$ active species under operational OER conditions, along with the formation of the Co superoxide intermediate. Beyond OER applications, the Co_9S_8-derived active phase demonstrated notable efficiency in catalyzing the selective oxidation of biomass-derived glycerol and furan-2-carboxaldehyde to formate and furan-2-carboxylic acid, respectively, achieving yields exceeding 80%, with excellent reusability. A full hybrid-water electrolysis cell has been developed, wherein biomass valorization with Co_9S_8, coupled with H_2 production, resulted in a significant improvement in energy efficiency compared to conventional water-splitting.

Received 3rd August 2024
Accepted 5th October 2024

DOI: 10.1039/d4ta05436a

rsc.li/materials-a

1 Introduction

The development of a sustainable, carbon-neutral energy economy in the future necessitates the efficient production of green hydrogen, and hydrocarbon-based fuels/chemicals *via* the renewable energy-driven electrocatalytic reduction of water and carbon dioxide, respectively.[1,2] These crucial cathodic processes rely on the oxygen evolution reaction (OER) at the anode to provide the required protons and electrons.[2,3] However, the efficiency of the OER is severely hampered by its sluggish kinetics resulting from four electron/proton transfer steps, thereby limiting the industrial viability of these fuel-forming electrolyzers.[4,5] This has prompted the development of a wide range of highly active and durable OER electrocatalysts based on transition metals (TMs), as their cost-effectiveness, earth-abundance, and non-toxic nature render them well-suited for large-scale applications.[6–8]

In the field of TM-based electrocatalysts, cobalt (Co)-based materials exhibit remarkable versatility across various compositions including chalcogenides, pnictides, oxides, layered double hydroxides, cobaltites, borophosphates, intermetallics, and more, demonstrating remarkable efficiency in the practical OER.[8–13] Among these materials, cobalt chalcogenides, especially sulfides have emerged as compelling OER (pre)catalysts, owing to their substantially lower cost and reduced toxicity compared to other chalcogenides such as selenides and tellurides.[14] Furthermore, their phases, morphologies, compositions

[a]Department of Chemistry: Metalorganics and Inorganic Materials, Technische Universität Berlin, Straße des 17 Juni 115, Sekr. C2, 10623 Berlin, Germany. E-mail: prashanth.menezes@mailbox.tu-berlin.de

[b]Materials Chemistry Group for Thin Film Catalysis – CatLab, Helmholtz-Zentrum Berlin für Materialien und Energie, Albert-Einstein-Str. 15, 12489 Berlin, Germany. E-mail: prashanth.menezes@helmholtz-berlin.de

[c]Department of Chemistry: Biophysical Chemistry, Technische Universität Berlin, Straße des 17 Juni 115, Secr. PC14, 10623 Berlin, Germany

† Electronic supplementary information (ESI) available. CCDC 2338752. For ESI and crystallographic data in CIF or other electronic format see DOI: https://doi.org/10.1039/d4ta05436a

and surface and electronic properties can be readily fine-tuned for achieving high catalytic activities.[15–19] Typically serving as (pre)catalysts, Co sulfide materials undergo either surface, partial, or complete reconstruction under alkaline anodic potentials, wherein S leaches out as water-soluble (oxy)anions SO_4^{2-} and SO_4^{3-}, and a stable Co^{III} oxyhydroxide (CoO_xH_y) active phase is formed.[13,14,20–23] This anion leaching process induces porosity and defects and exposes more active sites in the transformed catalyst, resulting in significantly higher activities compared to oxyhydroxide phases obtained without sacrificial elements.[23–25] Under *operando* conditions, these $Co^{III}OOH$ active phases oxidize to form higher-valent Co^{IV}–O species, as well as the active oxygen species, Co superoxide, which has seldom been captured *via in situ* techniques.[21,26–28] Moreover, recent *in situ* studies have revealed residual sulfide species on the surface of the transformed catalyst, likely attributed to the adsorption of thermodynamically stable oxyanions.[29,30] This phenomenon can tune the catalyst's electronic properties to stabilize the OER intermediates and break the *OH/*OOH scaling relations, thereby amplifying the OER activity.[30,31] Therefore, the advancement of Co sulfide materials, and the detection of their true active structures and key intermediates for the OER is of utmost importance for the future development of this field.

In this regard, among the diverse range of Co sulfides investigated for the OER, phases such as Co_9S_8 and Co_4S_3 are of particular significance since their Co-rich crystal structures endow the *in situ* derived CoO_xH_y active phases with a high number of redox-active Co sites, thereby promoting significantly enhanced activities.[15–19] Several Co_9S_8-based materials including pristine Co_9S_8 nanoparticles, Co_9S_8-based heterostructures, hierarchical nanostructures, layer-double hydroxides, hybrid materials, heteroatom doped structures, and Co_9S_8 supported or grown *in situ* on conductive supports like graphene, metal foams, *etc.* have been developed in recent years, and they have shown excellent OER activities and long-term stabilities, surpassing the state-of-the-art noble-metal based catalysts RuO_2 and IrO_2, as well as other Co oxide catalysts.[15–19] However, the synthesis of such phases usually involves high-temperature solid-state methods, with prolonged reaction times, potentially resulting in the formation of particles with large and non-uniform sizes.[15,32] Therefore, the development of energy-efficient synthetic strategies to access Co-rich sulfide phases is highly crucial. To circumvent these challenges, the solvent-mediated single-source precursor (SSP) provides a viable alternative, involving the careful design of a precursor to enable direct access to a Co-rich sulfide phase with uniform nanosized particles, at relatively low temperatures and shorter reaction times.[32–34] In this context, the 2-mercaptopyridine ligand-supported transition-metal (TM) complexes have proven to be excellent precursors for the synthesis of TM sulfides under comparably mild conditions,[35–37] where the Cu-2-mercaptopyridine complex can effortlessly yield the challenging Cu-rich Cu_9S_5 phase.[36] This motivation drove us to synthesize a novel molecular complex incorporating a 2-mercaptopyridine ligand with cobalt and to investigate its potential for obtaining a thermodynamically challenging cobalt sulfide phase.

On the other hand, to enhance the efficiency of the known water-splitting reaction and to overcome the kinetic and thermodynamic barriers associated with the overall water splitting, the cell-potentials of electrolyzers should be significantly reduced by substituting the OER with organic oxidation reactions (OORs), a concept known as hybrid water electrolysis (HWE).[38,39] This approach not only reduces energy requirements but also enables the production of value-added products at the anode, diverging from the low-value oxygen generated in the conventional OER. Incidentally, earth-abundant and inexpensive biomass has emerged as a sustainable and carbon-neutral feedstock for the synthesis of valuable commercial products.[40–42] In this regard, Co-based materials have demonstrated promising results for the oxidation of a wide range of biomass-derived chemicals such as methanol, ethanol, glycerol, glucose, furfural, 5-hydroxymethylfurfural, *etc.*, into value-added products with high FEs.[43–51] However they still remain much less explored compared to Ni and NiFe-based electrocatalysts, which have been extensively studied for HWE in recent years.[38,52–54] Similar to the OER, Co-rich sulfide phases such as Co_9S_8 have particularly shown superior performance for the oxidation of organics.[55–57] Therefore, the development of such phases with effective applicability in upgrading/valorizing organic compounds is the need of the hour and holds significant importance in HWE. Furthermore, since similar active sites are responsible for catalyzing both the OER and OOR,[53,58] a systematic investigation interconnecting the two reactions is critical from a fundamental point of view.

Inspired by the challenges outlined above, the current study aims to address and answer the following research questions: (i) Can a novel molecular precursor be rationally designed to access a Co-rich sulfide phase? (ii) Does this material exhibit efficient performance for the OER? (iii) What constitutes the active structure of the material, and what are the factors influencing its activity?. And finally, (iv) can this material be effectively utilized for the selective oxidation of organic substrates to yield value-added industrial products and improve the energy efficiency of the water-splitting process?

In this study, we have designed a novel 2-mercaptopyridine ligand supported Co-complex, $[Co^{II}(PyHS)_4(OTf)_2]$, with triflate counter anions, employing a facile one-step protocol, and subsequently, we decomposed it using the hot-injection method at a low-temperature, resulting in the formation of a nanostructured Co_9S_8 phase. Notably, this phase exhibited remarkable activity and long-term durability for the OER, even at higher current densities. Detailed analyses, including comprehensive quasi *in situ* Raman spectroscopy coupled with *ex situ* characterization, revealed that Co_9S_8 underwent complete reconstruction into a nanocrystalline layered Co oxyhydroxide phase, with CoO_2 as the active species and Co superoxide as the plausible key OER intermediate. Moreover, we explored the applicability of the Co_9S_8 (pre)catalyst in two prominent OORs, demonstrating impressive performances in the selective valorization of glycerol and furfural to formate and 2-furoic acid, respectively.

2 Results and discussion

2.1 Synthesis and characterization of the $[Co^{II}(PyHS)_4(OTf)_2]$ precursor (1)

The novel molecular complex **1** was isolated in 90% yield as a green crystalline solid by treatment of cobalt(II) triflate with four molar equivalents of 2-mercaptopyridine in dichloromethane at room temperature, and under inert conditions (Fig. 1). Complex **1** is characterized by ^{1}H and ^{19}F nuclear magnetic resonance (NMR) spectroscopy, electrospray ionization mass spectrometry (ESI MS), Fourier transformed infrared spectroscopy (FT-IR), and single-crystal X-ray diffraction (scXRD) analysis. The ^{1}H NMR analysis unveiled the paramagnetic nature of the complex, and the FT-IR spectrum displayed peaks at 1132 and 1375 cm^{-1} characteristic of the ν(S=O) and ν(C–F) vibrations of the triflate counter anion, respectively (Fig. S1–S3†). The molecular structure of **1** established by scXRD analysis revealed a dicationic Co center coordinated to four terminal monodentate PyHS ligands (Fig. 1 and S4, Table S1†). The $[Co^{II}S_4]$ core adopts a distorted tetrahedral geometry, with Co–S bond distances of 2.2898(12)–2.2987(14) Å and S–Co–S bond angles in the range of 90.13(5)–121.83(6)°, which are in good agreement with those of previously reported metal sulfide complexes (Table S2†).[35–37]

2.2 Synthesis and characterization of Co_9S_8

The molecular complex **1** was subjected to hot-injection, at 260 °C in oleylamine, which yielded a gray colored powder. Analysis of the obtained material by powder X-ray diffraction (pXRD) revealed the formation of a phase pure of crystalline Co_9S_8 (JCPDS no 1-86-2273) (Fig. S5†). Co_9S_8 crystallizes in the cubic space group $Fm\bar{3}m$ (no. 225) with the lattice parameters a = 9.9230 (Å), V = 997.08 $Å^3$, and z = 4 (Fig. 1 and S6†). Herein, the body-centered Co is coordinated to six S atoms in an octahedral manner at a distance of 2.48 Å. The rest of the Co atoms are each coordinated to four S atoms in a tetrahedral manner at a distance of 2.14 Å.[59] Scanning electron microscopy (SEM) of Co_9S_8 unveiled the presence of agglomerates with hexagon-like morphology, and elemental mapping showed a homogenous distribution of Co and S throughout the sample, with an O content of <1% (Fig. 2a, b and S7†). The chemical composition of the material was corroborated by inductively coupled plasma optical emission spectroscopy (ICP-OES) and energy dispersive X-ray (EDX), quantifying a ratio of 1 : 0.89 for Co : S, consistent with its composition obtained from pXRD (Fig. S8 and Table S3†). The atomic structure of Co_9S_8 was elucidated through transmission electron microscopy (TEM), revealing hexagon-like particle aggregates (Fig. 2c and S9†). Moreover, the selected area electron diffraction (SAED) pattern exhibited distinct bright scattered spots, a characteristic indicative of crystalline material. Specifically, the (311), (331), (511), and (440) planes of Co_9S_8 could be identified from the SAED pattern (Fig. 2d).

X-ray photoelectron spectroscopy (XPS) was performed to identify the surface electronic structure of Co_9S_8. The deconvoluted Co 2p spectrum displayed two prominent peaks at 778.4 eV ($2p_{3/2}$) and 793.4 eV ($2p_{1/2}$), confirming the presence of low-valent Co associated with the Co–S bonds (Fig. 2e).[60,61] Additionally, two peaks at 779.9 eV ($2p_{3/2}$) and 795.5 eV ($2p_{1/2}$) were observed, attributed to Co^{II} species arising from surface passivation, consistent with previous literature.[60,61] Similarly, the deconvolution of the S 2p spectrum confirmed the presence of low-valent S peaks corresponding to the S–Co bonds, at 161.5 eV ($2p_{3/2}$) and 162.5 eV ($2p_{1/2}$), while slight surface passivation led to the formation of S–O bonds, with peaks at 166.4 eV ($2p_{3/2}$) and 167.7 eV ($2p_{1/2}$) (Fig. 2f).[61,62] Additionally, the formation of oxidized Co^{II} species on the surface creates Co deficiencies in the underlying Co–S phase, consequently enriching it with S and leading to the formation of a S_2^{2-}

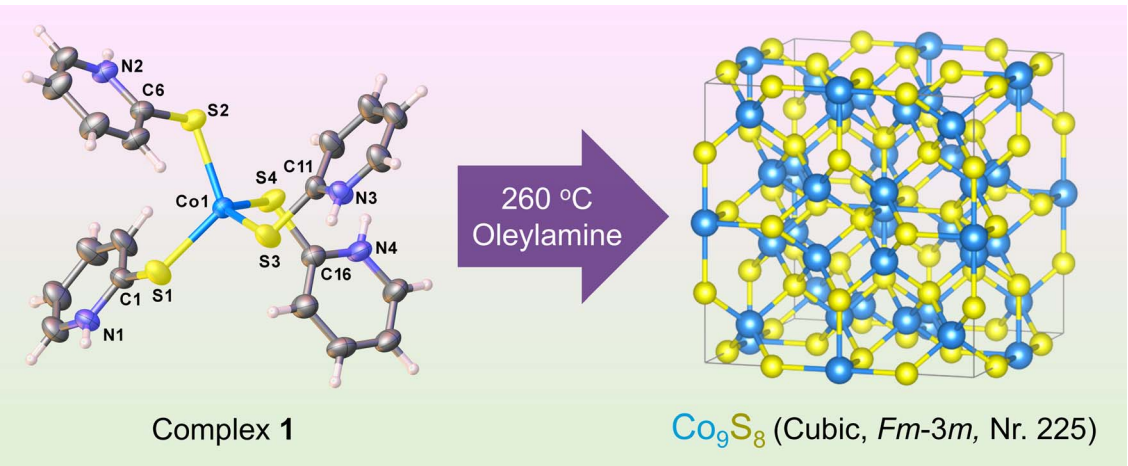

Fig. 1 Soft chemical approach towards material synthesis. Decomposition of complex **1**, $[Co^{II}(PyHS)_4(OTf)_2]$, using the hot-injection method in oleylamine produced the nanocrystalline Co_9S_8 phase. The molecular structure of complex **1** has been depicted with thermal ellipsoids at 50% probability. Triflate anions are omitted for clarity. Color code; cobalt: blue, sulfur: yellow, carbon: gray, and nitrogen: purple. CCDC 2338752 contains the supplementary crystallographic data for this paper. These data are provided free of charge by The Cambridge Crystallographic Data Centre.† The crystal structure of Co_9S_8 shows Co (blue) and S (yellow) in a unit cell (gray lines).

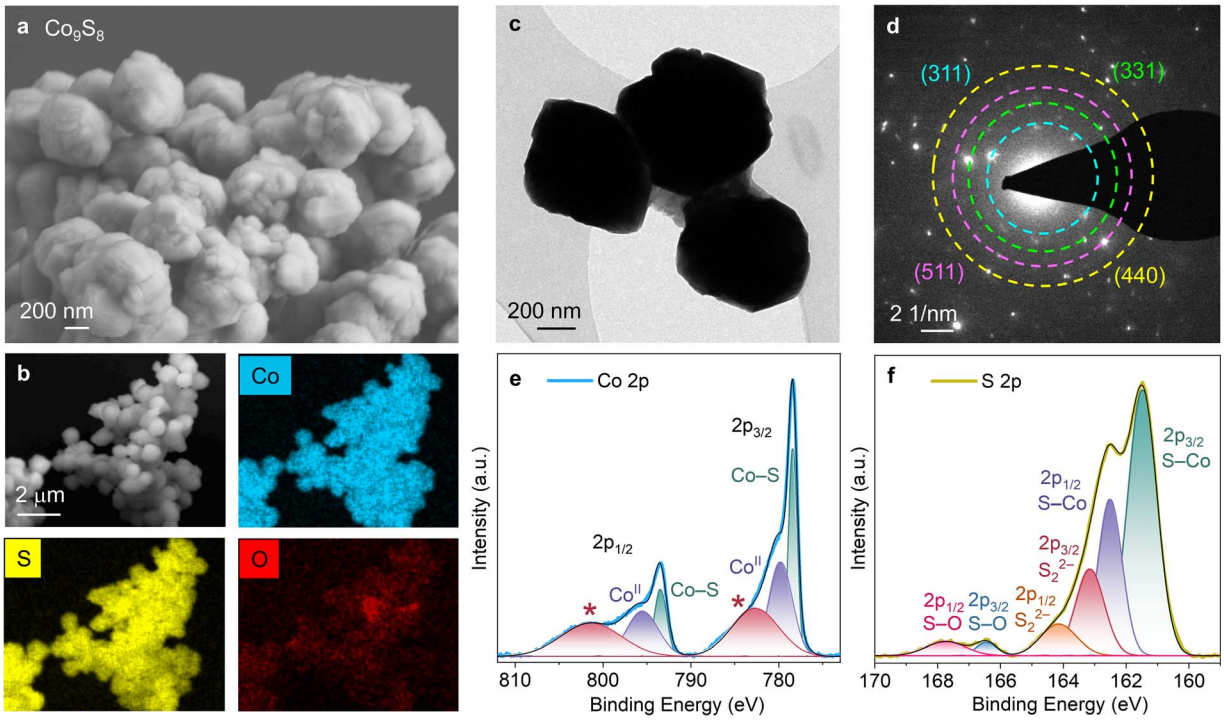

Fig. 2 Characterization of as-prepared Co_9S_8. (a) SEM image of Co_9S_8 displaying agglomerated particles and the corresponding (b) elemental mapping exhibiting a homogenous distribution of Co and S. The O content is <1% (c) TEM image of Co_9S_8 showing hexagon-like particles, and the corresponding (d) SAED pattern showing the diffraction rings of Co_9S_8 (JCPDS 1-86-2273). The deconvoluted (e) Co 2p and (f) S 2p XPS spectrum of Co_9S_8. Here asterisk (*) represents satellite peaks.

species, as evidenced by the peaks at 163.1 eV ($2p_{3/2}$) and 164.1 eV ($2p_{1/2}$).[35] The O XPS spectrum substantiates the presence of the above-mentioned surface oxidized species (Fig. S10†).[63]

Considering that oxyhydroxides represent the ultimate active structure for Co-based materials, we deliberately synthesized well-known reference materials such as CoOOH, alongside $Co(OH)_2$ and Co_3O_4 catalysts. This approach allows for the attained catalytic activities to be clearly benchmarked under identical conditions. All the obtained materials exhibited crystalline purity, as confirmed from their pXRD patterns (Fig. S11–S13†).

2.3 Electrochemical alkaline OER measurements

To explore the electrochemical performance of Co_9S_8 and the reference materials for the OER, the as-synthesized samples were electrophoretically deposited onto fluorine-doped tin oxide (FTO) and nickel foam (NF) substrates, with mass loadings of 0.4 ± 0.1 mg cm^{-2} and 0.7 ± 0.1 mg cm^{-2}, respectively. The prepared films were thoroughly characterized by pXRD, SEM, elemental mapping, EDX, and ICP-AES, confirming the retention of the crystal structure, morphology and composition of the materials during the electrodeposition process (Fig. S14–S17 and Table S3†). They were subsequently employed as the working electrode in a three-electrode set-up for all electrochemical measurements. Initially, all the measurements were exclusively conducted on the inert FTO substrate, to elucidate the accurate performance parameters of these materials.

Prior to the OER measurements, the materials were activated through cyclic voltammetry (CV), with cycling continuing until the current responses reached a stable state (10 cycles between 0.9 and 1.65 V_{RHE}). All the materials displayed distinct Co^{II}/Co^{III} and Co^{III}/Co^{IV} redox features in their respective CV scans (Fig. S18†).[64] The OER activity of the materials was subsequently determined from their respective linear sweep voltammetry (LSV) curves (Fig. 3a).

Interestingly, Co_9S_8 exhibited the highest OER activity, attaining the benchmark current density of 10 mA cm^{-2} at a low overpotential (η) of 328 ± 4 mV, which aligns well with the activities of other reported cobalt sulfide materials (Tables S4 and S5†). Conversely, $Co(OH)_2$, CoOOH, and Co_3O_4 showed higher η_{10} values of 361 ± 2 mV, 405 ± 3 mV, and 507 ± 5 mV, respectively. Moreover, the Nyquist plots derived from electrochemical impedance spectroscopy (EIS) displayed a consistent correlation between the resistance to charge transfer (R_{ct}) values of the materials and their OER activities, wherein the lowest R_{ct} value was attained for Co_9S_8 (Fig. 3b and Table S6†).

The materials were further investigated to determine the number of active Co sites, which can be estimated by quantifying the number of electrons transferred in their respective Co-redox features.[65] This quantification was achieved by integrating the redox peaks in the cathodic sweep of their CVs (Fig. S18†). Herein, Co_9S_8 exhibited a higher number of moles of redox-active electrons (0.29 μmol), compared to $Co(OH)_2$ (0.20 μmol), CoOOH (0.13 μmol), and Co_3O_4 (0.23 μmol), indicating the presence of a higher number of Co-redox active sites in

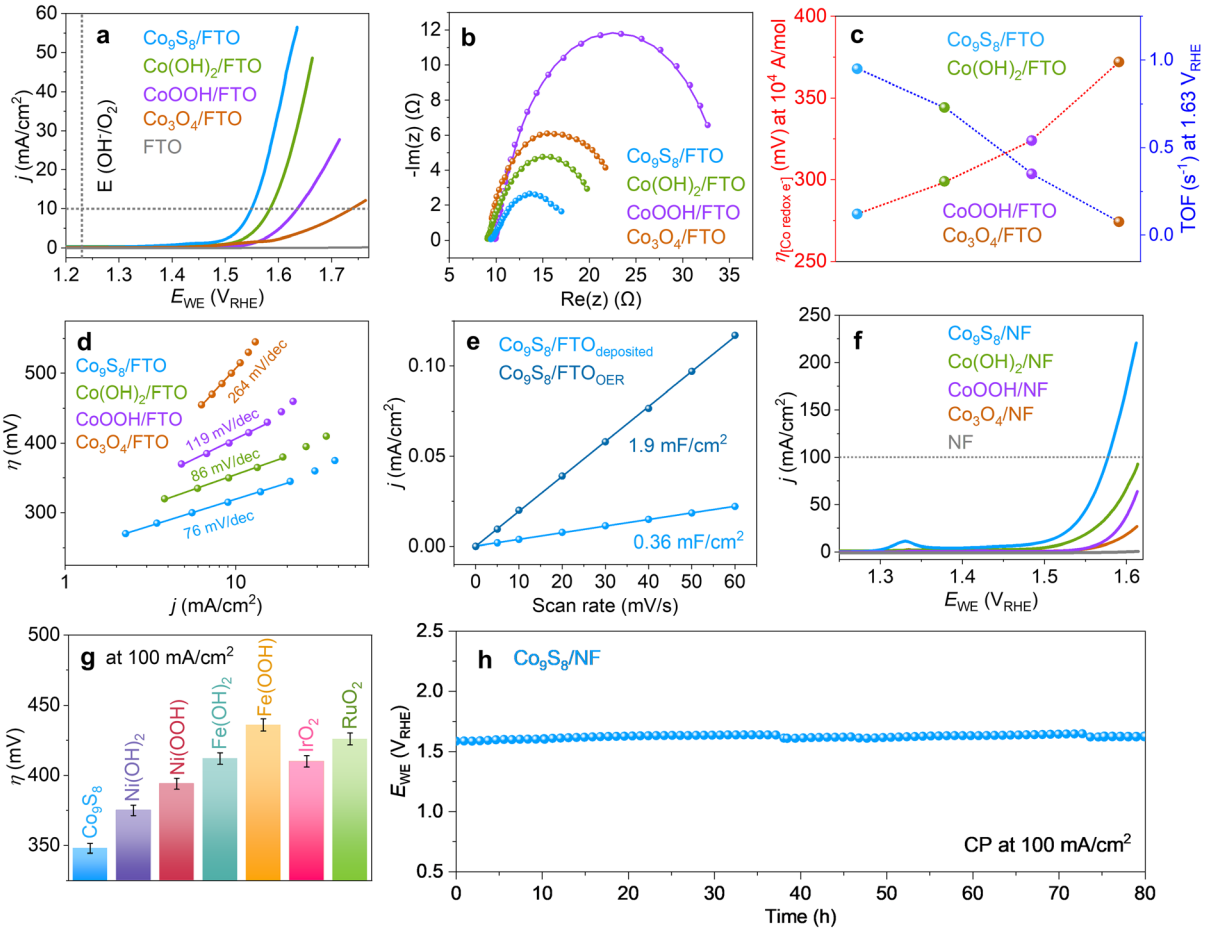

Fig. 3 Assessment of the OER performances of the catalysts. All the measurements are performed in 1 M KOH at 25 °C, with 90% *iR* correction. (a) LSV curves (at 5 mV s^{-1}) of Co_9S_8, $Co(OH)_2$, CoOOH, and Co_3O_4 on FTO and bare FTO, and their corresponding (b) Nyquist plots (obtained from EIS), (c) η values at 10^4 A mol^{-1} obtained from the activities normalized by the corresponding number of redox-active electrons (Fig. S19†); TOFs, and (d) Tafel slopes (recorded using steady-state CA measurements). (e) C_{dl} values of as-deposited Co_9S_8 on FTO and after 24 h CP at 10 mA cm^{-2} (f) LSV curves (at 3 mV s^{-1}) of the catalysts on NF and bare NF. (g) Comparison of the OER activity of Co_9S_8 with those of other established catalysts under the same working conditions (on a NF substrate). (h) CP of Co_9S_8/NF at 100 mA cm^{-2} showing stable performance for 80 h.

Co_9S_8, coherent with its higher OER activity. Normalization of the LSVs of the materials with their given number of redox-active electrons evidenced that Co_9S_8 also holds the highest intrinsic activity among the examined materials (Fig. 3c and S19†). A more precise insight into the intrinsic activity trend of the materials can be obtained from their turnover frequency (TOF) values:[65,66] Notably, Co_9S_8 demonstrates the highest TOF (0.95 s^{-1}), followed by $Co(OH)_2$ (0.73 s^{-1}), CoOOH (0.35 s^{-1}), and Co_3O_4 (0.076 s^{-1}) (Fig. 3c and Table S7†). Furthermore, the lowest Tafel slope was obtained for Co_9S_8 (76 ± 2 mV dec^{-1}) as compared to $Co(OH)_2$ (86 ± 2 mV dec^{-1}), CoOOH (119 ± 4 mV dec^{-1}), and Co_3O_4 (264 ± 8 mV dec^{-1}), implying that Co_9S_8 has the fastest OER kinetics among all the investigated catalysts (Fig. 3d).[67]

Furthermore, the change in the electrochemical surface area (ECSA) of Co_9S_8 during the OER was estimated by measuring the double-layer capacitance (C_{dl}) values of the as-deposited Co_9S_8 on FTO and after chronopotentiometry (CP) at 10 mA cm^{-2} for 24 h (Fig. S20†), since ECSA is directly proportional to C_{dl} (Fig. 3e and S21†).[68] As expected, an increase in the C_{dl} value, from 0.36 mF cm^{-2} to 1.9 mF cm^{-2}, was observed, indicating a transformation of the material during the OER. However, it should be noted here that the C_{dl} measurements are subject to high uncertainty due to conductivity limitations, as outlined in previous reports.[69–71]

Motivated by these results and in the pursuit of enhancing OER performances to achieve industrially relevant benchmarks, we employed a conductive, high surface area and porous NF substrate.[58,72–74] Remarkably, this led to a significant enhancement in the activity of Co_9S_8, requiring an η_{10} of only 258 ± 3 mV to yield a current density of 10 mA cm^{-2} (Fig. 3f and Table S4†). Subsequently, an activity trend of Co_9S_8 > $Co(OH)_2$ (298 ± 3 mV) > CoOOH (340 ± 3 mV) > Co_3O_4 (352 ± 4 mV) was recorded, aligning with the trend observed on FTO. The activity of Co_9S_8 surpasses that of other state-of-the-art noble and transition metal-based catalysts ($Ni(OH)_2$, NiOOH, $Fe(OH)_2$, FeOOH, IrO_2, and RuO_2) tested under identical working conditions, as well as other reported cobalt sulfide materials

investigated for the OER (Fig. 3g and S22, Table S5†). Moreover, an OER faradaic efficiency (FE) of 96 ± 3% was attained for Co_9S_8/NF (Table S8†), and upon subjecting it to a high current density of 100 mA cm^{-2}, it exhibited stable performance, maintaining an overpotential of 348 mV over 80 h (Fig. 3h).

2.4 *Ex situ* post-OER characterization

To gain a comprehensive understanding of the active structure of Co_9S_8 for the OER, a series of characterization studies were performed following a 24 h treatment of the FTO film at 10 mA cm^{-2} (Fig. S20†). Interestingly, SEM revealed a complete transformation of the hexagon-like morphology of Co_9S_8, evolving into an irregular triangular morphology after the OER (Fig. S23†). Additionally, elemental mapping unveiled a homogenous distribution of Co and O in the material after the OER, accompanied by a drastic loss of S, as confirmed by the Co : S ratio of 1 : 0.01, determined through ICP-OES and EDX analysis (Fig. S24, S25 and Table S3†). Furthermore, the structural transformation of Co_9S_8 post-OER was examined by TEM, confirming a complete reconstruction from the initially hexagon-like shape to a triangle-like shape (Fig. 4a and S26a†). HR-TEM uncovered the formation of a sheet-like structure (Fig. 4b and S26b, S26c†), while the distances of the rings in the corresponding SAED patterns, measured at 1.2, 1.4, 2.0, and 2.4 Å (Fig. 4c), align well with the expected layered oxyhydroxide phases, strongly suggesting the emergence of a CoOOH phase during the OER.[13]

The changes in the surface electronic structure of Co_9S_8 during the OER were investigated through XPS. The post-OER deconvoluted Co 2p spectrum revealed the complete oxidation of the low-valent Co species associated with the Co_9S_8 phase, into higher oxidation state species, Co^{III} (at 780.4 eV $2p_{3/2}$ and 795.3 eV $2p_{1/2}$) and Co^{II} (at 783.0 eV $2p_{3/2}$ and 797.6 eV $2p_{1/2}$).[75] The $2p_{3/2}$ and $2p_{1/2}$ spin–orbit coupling of ~15 eV correlates to a higher amount of Co^{III} species, attributed to the formation of the CoOOH phase during the OER (Fig. 4d).[75] Likewise, the post-OER S 2p spectrum does not display any metal bonded S (between 161 and 163 eV) confirming the absence of Co_9S_8 species. Instead, it exhibited a peak at 168.6 eV, which could be attributed to surface adsorbed SO_4^{2-} species (Fig. 4e).[76] The O 1s XPS spectrum displays peaks corresponding to the M–O bonds (O1) and hydroxides/(oxy)hydroxides (O2), which unequivocally confirms the formation of the aforementioned oxidic species after the OER (Fig. 4f).[77] It also indicates the presence of a minor amount of adsorbed water molecules (O3).[77]

2.5 Quasi *in situ* Raman spectroscopy

To shed light on the true active structure of Co_9S_8 under OER operating conditions, quasi *in situ* Raman spectroscopy was performed. For this purpose, the Co_9S_8/FTO sample was rapidly freeze-quenched in liquid N_2 at a working potential of 1.56 V_{RHE} after being subjected to a current density of 10 mA cm^{-2} for 24 h. The Raman spectrum of as-prepared Co_9S_8 evolves into

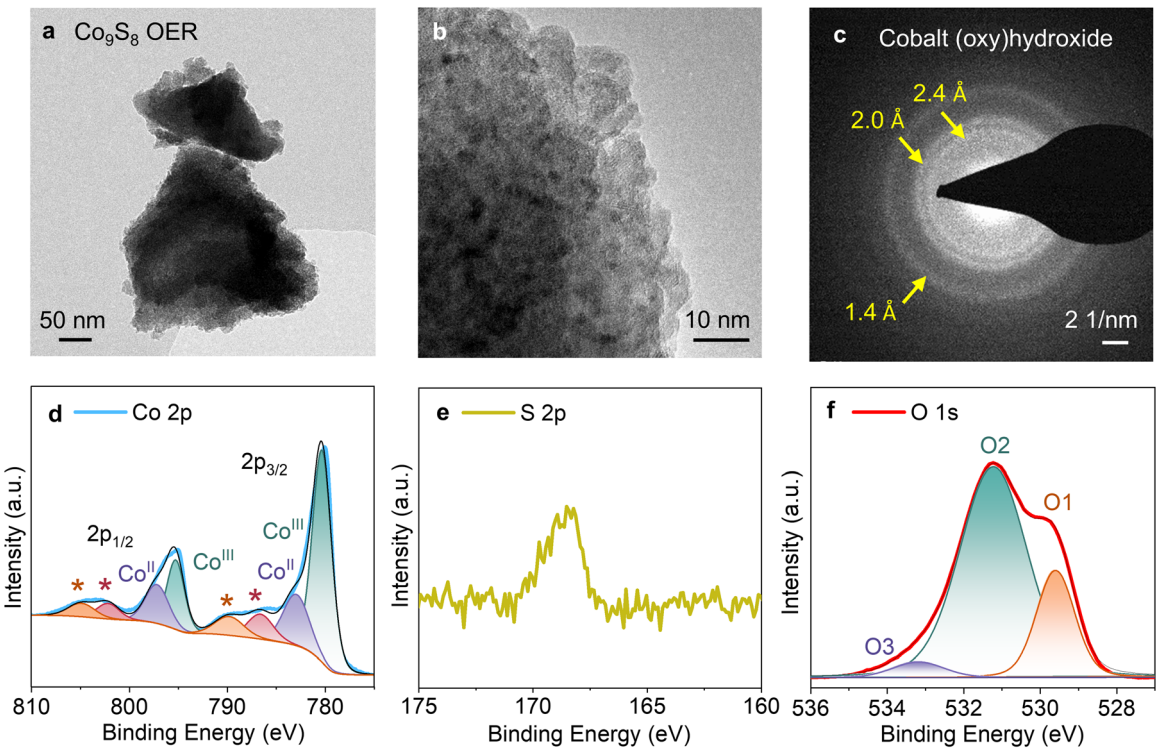

Fig. 4 *Ex situ* characterization of Co_9S_8 post-OER. All the characterization studies were performed after treating the sample for 24 h at 10 mA cm^{-2} on FTO, in 1 M KOH. The post-OER (a) TEM, (b) HR-TEM, (c) SAED, and the deconvoluted (d) Co 2p, (e) S 2p and (f) O 1s XPS spectra, corroborate the complete transformation of Co_9S_8 into a CoOOH active phase during the OER. Here asterisk (*) represents satellite peaks.

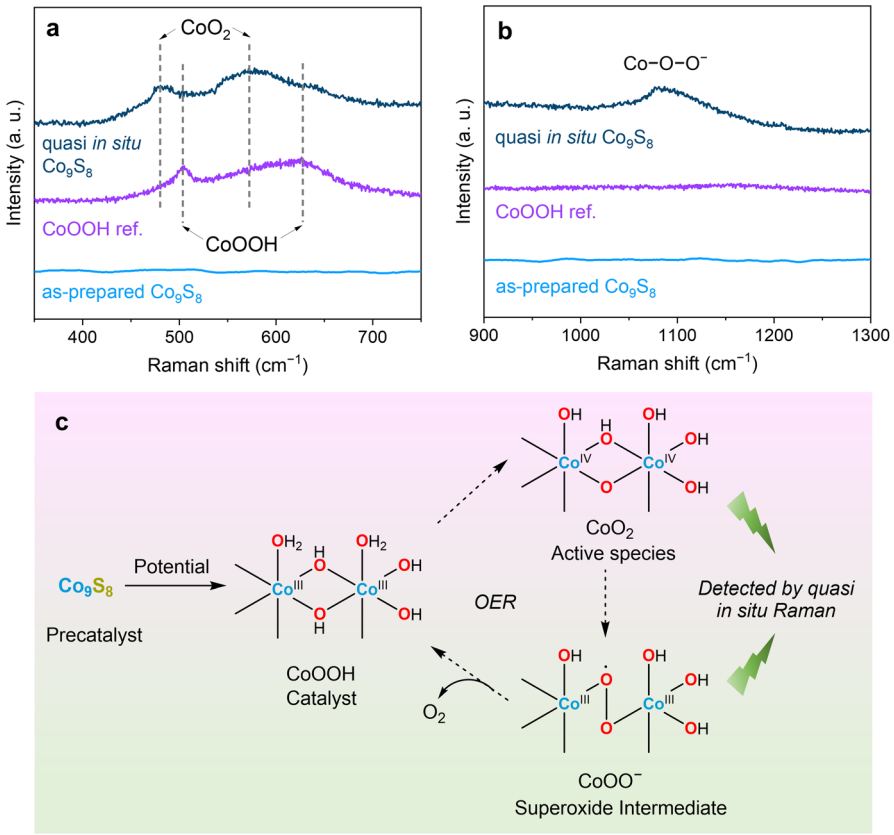

Fig. 5 Quasi *in situ* Raman spectroscopic data and schematic representation of the active species and plausible intermediate. (a and b) Raman spectroscopic data of the as-prepared Co_9S_8 and CoOOH reference powders, and the quasi *in situ* OER Co_9S_8 sample, freeze quenched at 1.56 V_{RHE} displayed in different potential regimes. (c) Overview of the reconstruction, active catalyst, *in situ* detected active species and a proposed intermediate of Co_9S_8 for the OER by Raman spectroscopy.[21]

two distinct bands at ~478 and ~570 cm^{-1} under quasi *in situ* OER conditions (Fig. 5a). Compared with the bands at ~504 (E_g) and ~628 cm^{-1} (A_{1g}) in the Raman spectrum of the as-prepared CoOOH reference sample, the bands for quasi *in situ* Co_9S_8 are shifted to a lower wavenumber and are characteristic of the E_g and A_{1g} vibrational modes of the high-valency Co(IV) species, CoO_2.[21,50,51] Moreover, a broad peak emerged at ~1077 cm^{-1}, indicative of the formation of an active oxygen species, namely, Co superoxide (Fig. 5b).[21] As anticipated, the aforementioned peak was absent in the as-prepared Co_9S_8 and CoOOH powders.

Furthermore, the stability of the prepared Co_9S_8 phase was tested in 1 M KOH, without any applied potential. After 2 h of exposure, the pXRD analysis revealed no discernible change in the crystalline structure of the material (Fig. S27†). Moreover, the morphology, Co, and S mapping, and the Co : S ratio of 1 : 0.89 were also preserved after the treatment (Fig. S28 and S29†). This underlines that the material undergoes transformation solely when subjected to an anodic potential.

2.6 Active structure and catalytic activity of Co_9S_8 for the OER

Herein, the *ex situ* investigations reveal that under anodic potential in an alkaline environment, S leaches from Co_9S_8 and dissolves into the electrolyte as water-soluble oxyanions, which is accompanied by oxygen substitution to form the stable $Co^{III}OOH$ active phase (Fig. 5c). The CoOOH phase consists of layers formed by edge-sharing [CoO_6] octahedra.[11] The leaching of S generates a large number of voids, enabling greater electrolyte penetration, thus enriching the *in situ* formed CoOOH catalyst with a high number of Co active sites (Fig. S18†), and a high ECSA (Fig. 3e). As a result, Co_9S_8 demonstrates a superior OER performance compared to the as-prepared, direct CoOOH, $Co(OH)_2$, and Co_3O_4 catalysts.

Intriguingly, the quasi *in situ* Raman analysis reveals that this CoOOH active phase evolves into disordered CoO_2 containing higher oxidation state Co(IV), under OER operating potential (Fig. 5c).[21,50,51] Moysiadou *et al.* showed that this active species serves as the dominant resting state of the CoOOH catalyst under *operando* conditions.[21] Furthermore, they reported that the broad band observed between 900 and 1300 cm^{-1} is for a Co superoxide species, a key OER intermediate, similar to the active oxygen species observed for nickel and nickel-iron oxyhydroxides.[21,35,77] This superoxide species has seldom been captured previously for other Co-based materials.[26–28] The release of dioxygen from this superoxide species has been proposed as the rate-determining step for the OER.[21]

Furthermore, as mentioned above, the Co-rich structure of the Co_9S_8 phase provides its *in situ* derived active phase with

a greater number of active sites, which contributes to its enhanced activity. To substantiate this, we prepared a CoS phase, with a 1 : 1 ratio of Co : S from the same precursor (complex **1**), using the hot-injection method at a lower temperature, 225 °C (Fig. S30†). The Co_9S_8 phase showed significantly higher catalytic activity compared to the CoS phase, thus confirming the superiority of the former for the OER (Fig. S32†).

Lastly, to comprehend if the adopted SSP synthetic route confers any advantages to the catalytic activity, we synthesized a Co_9S_8 phase *via* a hydrothermal approach (Fig. S31†). Interestingly, the SSP-derived Co_9S_8 phase exhibited higher activity than the hydrothermally derived one, reiterating the advantages of the molecular SSP approach to material synthesis (Fig. S32†).

2.7 Hydrogen production coupled with biomass valorization

The Co_9S_8 (pre)catalyst was further employed for the selective anodic oxidation of biomass-derived glycerol and furfural (Fig. 6a). The selective oxidation of glycerol to C1 formic acid, rather than yielding CO_2 or less valuable C_2/C_3 products, holds significant commercial promise for its utilization as a fuel, raw material for organic synthesis, additive in rubber industries, and as an industrial solvent.[78,79] Similarly, selectively oxidizing furan-2-carboxaldehyde (furfural) to produce furan-2-carboxylic acid (2-furoic acid), could offer economic benefits by providing precursors for manifold applications in pharmaceuticals, agrochemicals, optics, food, and fragrance industries.[80,81] To accomplish this, the Co_9S_8 material on NF was initially activated through CV cycling in 1 M KOH until stable current responses were achieved (10 cycles between 0.9 and 1.65 V_{RHE}). Subsequently, LSV measurements were recorded in 1 M KOH, both in the absence and presence of 0.1 M glycerol/furfural (Fig. 6b). Interestingly, in the presence of organic substrates, the onset potential decreased to ~1.30 V_{RHE}, compared to the response observed with pure KOH (~1.45 V_{RHE}). Furthermore, a significant increase in the current response is observed, wherein a current density of 100 mA cm^{-2} is attained at significantly lower overpotentials of 175 mV and 286 mV for glycerol and furfural oxidation, respectively, compared to the OER (348 mV).

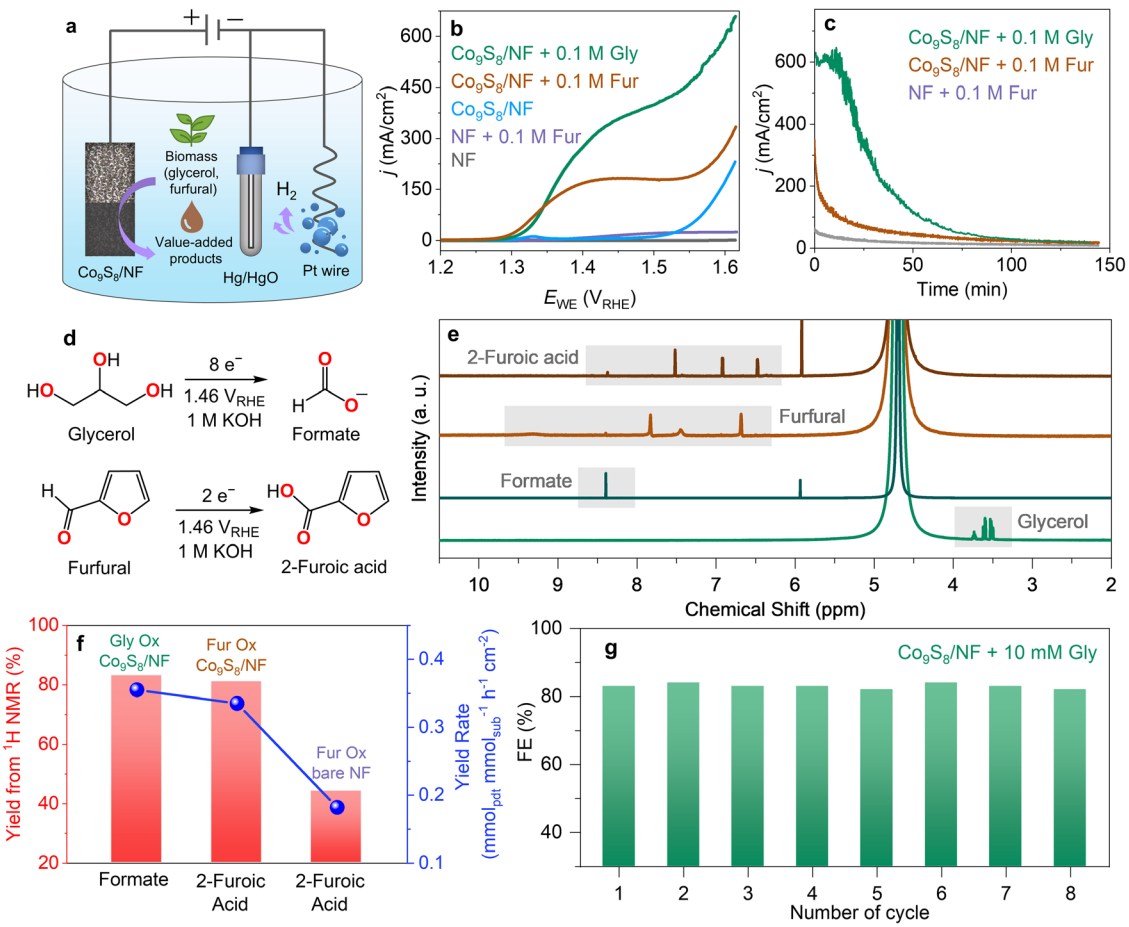

Fig. 6 Electrochemical upgrading of biomass-derived chemicals. (a) Schematic representation of the oxidation of glycerol, and furfural to value-added products with Co_9S_8/NF. (b) LSV curves (at 5 mV s^{-1}) of Co_9S_8/NF and bare NF in 1 M KOH in the absence and presence of 0.1 M glycerol (Gly)/furfural (Fur). (c) CA curve for the bulk electrolysis of 0.1 M glycerol, and furfural in 15 ml of 1 M KOH at 1.46 V_{RHE} to (d) selectively form formate and 2-furoic acid, respectively. (e) ^{1}H NMR spectrum of reaction mixtures before and after glycerol/furfural bulk oxidations with Co_9S_8/NF, and their corresponding (f) product yields and yield rates. (g) The FEs calculated during the bulk electrolysis of 10 mM glycerol in 15 ml of 1 M KOH at 1.46 V_{RHE} for 8 consecutive CA cycles.

The preceding results motivated us to conduct bulk electrolysis of glycerol and furfural with Co_9S_8/NF, aiming to obtain quantitative knowledge of their corresponding oxidation products. For this purpose, chronoamperometry (CA) was first performed at different potentials (1.35, 1.40, 1.46, and 1.50 V_{RHE}) with 0.1 M glycerol/furfural (in 15 ml of 1 M KOH) in the region where OOR predominantly occurs, with negligible OER current density, to find the optimum potential at which the FE is maximum for the two reactions (Fig. S33 and S34†). After 1 hour of glycerol and furfural oxidation electrolysis, the FEs were calculated from the corresponding ^{1}H NMR yields of the selectively obtained value-added products formate and 2-furoic acid, respectively, and quantified against maleic acid as an internal standard. The highest FE was obtained at 1.46 V_{RHE} for both reactions, with values of 83% and 81% for glycerol and furfural oxidations, respectively. Therefore, the bulk organic electrolysis was further conducted at 1.46 V_{RHE} until the charge required for the full conversion of glycerol to formic acid (1157.82 C in 140 min) and furfural to 2-furoic acid (289.45 C in 145 min) was passed, in order to quantify the bulk product yields (Fig. 6c). The ^{1}H NMR of the electrolytes recorded after the CAs revealed the product yield of formate to be 83% and that of 2-furoic acid to be 81% (Fig. 6d–f and S35, S37†). The yield rate of formate was found to be 0.355 $mmol_{formate}$ $mmol_{glycerol}^{-1}$ h^{-1} cm^{-2} and that of 2-furoic acid was found to be 0.335 $mmol_{2\text{-furioic acid}}$ $mmol_{furfural}^{-1}$ h^{-1} cm^{-2} (Fig. 6f). The performance of Co_9S_8/NF for both the reactions is comparable to those observed for other materials in the literature, highlighting the importance of our findings (Tables S9 and S10†). Importantly, for glycerol oxidation, carbonates or other C-based intermediates or products were not formed, as confirmed by the post-CA ^{13}C NMR analysis (Fig. S36†). Analogous control experiments were conducted with bare NF for furfural oxidation, demonstrating significantly lower current densities compared to those observed with Co_9S_8/NF, as evidenced by both LSV and CA measurements (Fig. 5b and c). Moreover, after bulk electrolysis with furfural for 145 min, ^{1}H NMR revealed a 44% yield of 2-furoic acid, with a yield rate 0.182 $mmol_{2\text{-furoic acid}}$ $mmol_{furfural}^{-1}$ h^{-1} cm^{-2} (Fig. 6f and S38†).

To test the reusability of Co_9S_8/NF for biomass valorization, consecutive CA bulk electrolysis measurements were conducted for glycerol oxidation (Fig. S39†). Interestingly, Co_9S_8/NF maintained the selective formation of formate with a FE of ~83% over 8 consecutive cycles (Fig. 6g and S40†). Furthermore, after the 8th cycle, only a slight decrease in the current density is observed from LSV curves (Fig. S41†). Therefore, overall, the results demonstrate that Co_9S_8 is a highly efficient catalyst for the selective electrooxidation of glycerol and furfural. It is well-known that similar active sites are responsible for catalyzing both the OER and OOR.[53,58] As described in Section 2.6, under the applied anodic potentials, S is completely leached from the

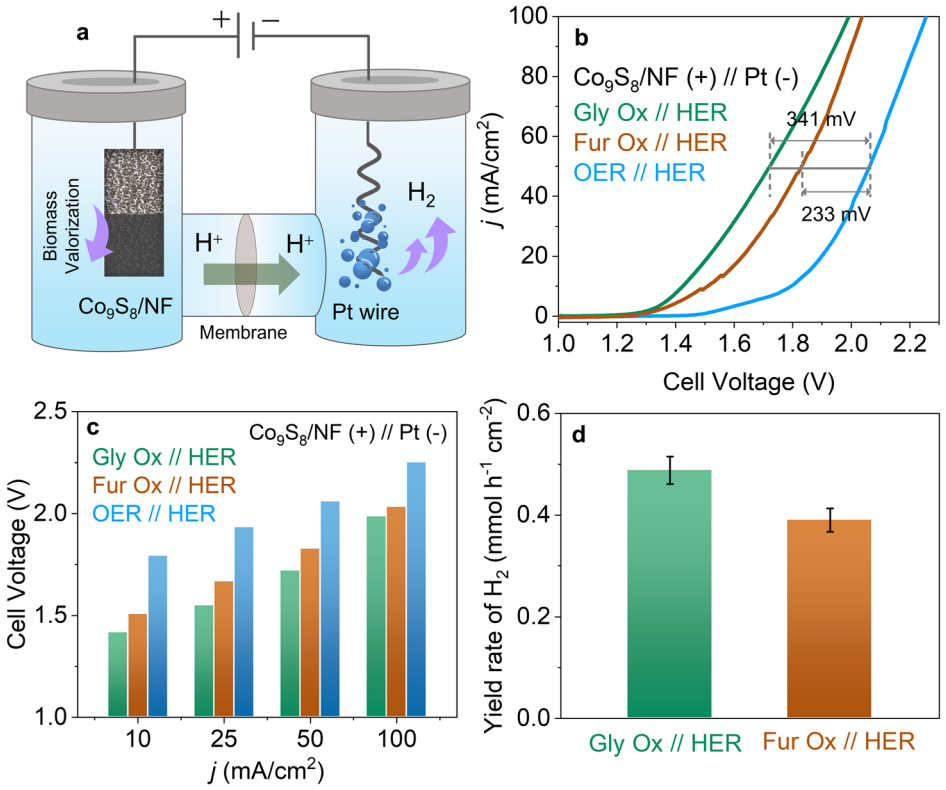

Fig. 7 Hybrid water electrolysis. (a) Schematic representation of biomass valorization at the Co_9S_8/NF anode coupled with the HER at the Pt wire cathode in a divided cell with a 2-electrode set-up. The anodic and cathodic chambers are separated by an anion exchange membrane. (b) LSV curves (at 5 mV s^{-1}) of the HWE cell in 1 M KOH in the absence and presence of 0.1 M glycerol (Gly)/furfural (Fur) in the anodic chamber, and (c) the corresponding cell voltages recorded for different current densities. (d) The FEs and yield rate of H_2 for the HER half-cell coupled with glycerol and furfural oxidations.

Co_9S_8 (pre)catalyst and a resultant $Co^{III}OOH$ active catalyst is formed. The S-leaching makes the active catalyst porous and enriches it with a high number of Co-redox sites (Fig. S18†) and a high ECSA (Fig. 3e). Furthermore, chalcogen leaching leads to an alteration of the electrode and reactant interface through the redistribution of the local charge, which has been proven to be beneficial for better migration of reactants during OORs.[76] Therefore, the *in situ* derived CoOOH active catalyst from Co_9S_8 exhibits high activities for the oxidation of organics as well, facilitating high yields and FEs.

Encouraged by the above findings, the oxidation of biomass on Co_9S_8/NF was further coupled with the hydrogen evolution reaction (HER) on Pt wire in a divided cell with a 2-electrode set-up to investigate the performance of the full HWE cell (Fig. 7a). Interestingly, the overall cell potential decreased substantially upon the addition of glycerol/furfural in the anodic half-cell (Fig. 7b). As shown in Fig. 7c, the cell voltages required to reach the current densities of 10, 25, 50 and 100 mA cm^{-2} were significantly lower in the presence of organic substrates. Specifically, at a current density of 50 mA cm^{-2}, the HWE cell required 341 mV (for glycerol oxidation) and 233 mV (for furfural oxidation) less potential than the overall water-splitting cell. Furthermore, bulk electrolysis was conducted for the HWE cells at 1.60 V and the FE and yield rate for both the half-cell reactions were calculated (Fig. S42a†). For the HER coupled with glycerol oxidation, the HER half-cell achieved a H_2 yield rate of 0.488 ± 0.026 mmol h^{-1} cm^{-2}, while for the HER coupled with furfural oxidation, the HER half-cell achieved a H_2 yield rate of 0.390 ± 0.022 mmol h^{-1} cm^{-2} (Fig. 7d and S42b†). For the glycerol and furfural oxidation half-cells, formate and 2-furoic acid were selectively produced with a FE of 80% and 79%, respectively. Therefore, the HWE cell significantly improved the energy efficiency while simultaneously producing H_2 at the cathode and value-added products at the Co_9S_8/NF anode with high FEs.

3 Conclusion

In conclusion, our study effectively addressed several key questions raised in the introduction of this work. First, we successfully synthesized a novel $[Co^{II}(PyHS)_4(OTf)_2]$ complex and utilized it to synthesize the nanocrystalline Co_9S_8 material using a soft chemical approach, thus addressing question (i). Secondly, concerning questions (ii) and (iii), our material demonstrated superior OER activity compared to other Co-based catalysts investigated in this study, as well as outperforming various Ni, Fe, and noble metal-based catalysts. Moreover, it displayed a remarkable FE of ~96% and long-term stability at 100 mA cm^{-2} towards the OER.

Extensive *ex situ* analyses confirmed that during the OER, Co_9S_8 underwent complete reconstruction into a CoOOH active phase *via* S-leaching, enhancing its ECSA, number of Co-redox active sites, and TOF. Quasi *in situ* Raman spectroscopy further suggested the presence of a higher valence state CoO_2 active species and a Co superoxide intermediate. Finally, addressing question (iv), this active phase also efficiently catalyzed the selective oxidation of glycerol and furfural to yield value-added products, namely, formate and 2-furoic acid, respectively. Furthermore, coupling the OOR with the HER significantly improved the energy efficiency of the cell in comparison to the conventional water-splitting process. Based on the insights gained from our study, we anticipate that the low-temperature SSP route can serve as an energy-efficient synthetic strategy for developing other thermodynamically challenging phases and other TM sulfide phases in general as electrodes for commercial water oxidation, as well as for facilitating large-scale production of value-added products in industries.

Data availability

The data supporting this article have been included as part of the ESI.†

Conflicts of interest

There are no conflicts to declare.

Acknowledgements

The project was funded by the German Federal Ministry of Education and Research in the framework of the project Catlab (03 EW0015A/B), project PrometH_2eus (03HY105C), and Deutsche Forschungsgemeinschaft (DFG, German Research Foundation) under Germany's Excellence Strategy – EXC 2008/1 – 390540038 – UniSysCat. The authors are indebted to Dr Lukas Reith (TU Berlin), Maria Unterweger (TU Berlin), the group of Prof. Dr Martin Lerch (TU Berlin), and Paula Nixdorf (TU Berlin) for their assistance in TEM, XPS, pXRD, and scXRD measurements, respectively. The authors are also thankful to Dr B. Chakraborty for introducing the 2-mercaptopyridine ligand for the synthesis of the molecular complex and Dr Shenglai Yao for helping in solving its crystal structure.

References

1 R. Schlögl, *Angew. Chem., Int. Ed.*, 2019, **58**, 343–348.
2 Z. W. Seh, J. Kibsgaard, C. F. Dickens, I. Chorkendorff, J. K. Nørskov and T. F. Jaramillo, *Science*, 2017, **355**, eaad4998.
3 X. Xie, L. Du, L. Yan, S. Park, Y. Qiu, J. Sokolowski, W. Wang, Y. Shao, X. Xie, L. Yan, S. Park, Y. Qiu, J. Sokolowski, W. Wang, Y. Shao and L. Du, *Adv. Funct. Mater.*, 2022, **32**, 2110036.
4 H. Yang, M. Driess and P. W. Menezes, *Adv. Energy Mater.*, 2021, **11**, 2102074.
5 H. Dau, C. Limberg, T. Reier, M. Risch, S. Roggan and P. Strasser, *ChemCatChem*, 2010, **2**, 724–761.
6 Y. Luo, Z. Zhang, M. Chhowalla and B. Liu, *Adv. Mater.*, 2022, **34**, 2108133.
7 K. Zhang, R. Zou, K. Zhang and R. Zou, *Small*, 2021, **17**, 2100129.
8 L. Han, S. Dong, E. Wang, L. Han, S. J. Dong, E. K. Wang and S. J. Dong, *Adv. Mater.*, 2016, **28**, 9266–9291.

9 S. Ghosh, A. Mondal, G. Tudu, S. Ghosh, H. V. S. R. M. Koppisetti, H. R. Inta, D. Saha and V. Mahalingam, *ACS Sustain. Chem. Eng.*, 2022, **10**, 7265–7276.
10 J. Wang, W. Cui, Q. Liu, Z. Xing, A. M. Asiri, X. Sun, J. Wang, W. Cui, Q. Liu, Z. Xing, X. Sun and A. M. Asiri, *Adv. Mater.*, 2016, **28**, 215–230.
11 P. W. Menezes, A. Indra, I. Zaharieva, C. Walter, S. Loos, S. Hoffmann, R. Schlögl, H. Dau and M. Driess, *Energy Environ. Sci.*, 2019, **12**, 988–999.
12 C. Walter, P. W. Menezes and M. Driess, *Chem. Sci.*, 2021, **12**, 8603–8631.
13 L. Reith, J. N. Hausmann, S. Mebs, I. Mondal, H. Dau, M. Driess and P. W. Menezes, *Adv. Energy Mater.*, 2023, **13**, 2203886.
14 J. N. Hausmann and P. W. Menezes, *Curr. Opin. Electrochem.*, 2022, **34**, 100991.
15 D. Dong, Z. Wu, J. Wang, G. Fu and Y. Tang, *J. Mater. Chem. A*, 2019, **7**, 16068–16088.
16 Y. Chang, Z. Ma, X. Lu, S. Wang, J. Bao, Y. Liu and C. Ma, *Angew. Chem., Int. Ed.*, 2023, **62**, e202310163.
17 Y. Pan, Y. Liu and C. Liu, *Appl. Surf. Sci.*, 2015, **357**, 1133–1140.
18 H. Li, X. Wu, P. Wang, S. Song, M. He, C. Li, W. Wang, Z. Fang, X. Yuan, W. Song and Z. Li, *ACS Sustain. Chem. Eng.*, 2022, **10**, 13112–13124.
19 S. Chakrabartty, S. Karmakar and C. R. Raj, *ACS Appl. Nano Mater.*, 2020, **3**, 11326–11334.
20 B. R. Wygant, K. Kawashima and C. B. Mullins, *ACS Energy Lett.*, 2018, **3**, 2956–2966.
21 A. Moysiadou, S. Lee, C.-S. Hsu, H. M. Chen and X. Hu, *J. Am. Chem. Soc.*, 2020, **142**, 11901–11914.
22 J. Masa and W. Schuhmann, *ChemCatChem*, 2019, **11**, 5842–5854.
23 X. Liu, J. Meng, J. Zhu, M. Huang, B. Wen, R. Guo and L. Mai, *Adv. Mater.*, 2021, **33**, e2007344.
24 Z. Chen, H. Yang, Z. Kang, M. Driess and P. W. Menezes, *Adv. Mater.*, 2022, **34**, 2108432.
25 H. Zhong, Q. Zhang, J. Yu, X. Zhang, C. Wu, Y. Ma, H. An, H. Wang, J. Zhang, X. Wang and J. Xue, *Adv. Energy Mater.*, 2023, **13**, 2301391.
26 X. Wang, J. Li, Q. Xue, X. Han, C. Xing, Z. Liang, P. Guardia, Y. Zuo, R. Du, L. Balcells, J. Arbiol, J. Llorca, X. Qi and A. Cabot, *ACS Nano*, 2023, **17**, 825–836.
27 X. Zhao, Y. Li, Y. Cui, M. Saqib, X. Zhang, R. Hao and Z. Zheng, *J. Am. Chem. Soc.*, 2023, **145**, 20897–20906.
28 M. Zhang, M. de Respinis and H. Frei, *Nat. Chem.*, 2014, **6**, 362–367.
29 N. C. S. Selvam, J. Lee, G. H. Choi, M. J. Oh, S. Xu, B. Lim and P. J. Yoo, *J. Mater. Chem. A*, 2019, **7**, 27383–27393.
30 J. N. Hausmann and P. W. Menezes, *Angew. Chem., Int. Ed.*, 2022, **61**, e202207279.
31 Y. Shi, W. Du, W. Zhou, C. Wang, S. Lu, S. Lu and B. Zhang, *Angew. Chem., Int. Ed.*, 2020, **59**, 22470–22474.
32 N. Kumar, N. Raman and A. Sundaresan, *Z. Anorg. Allg. Chem.*, 2014, **640**, 1069–1074.
33 C. Panda, P. W. Menezes and M. Driess, *Angew. Chem., Int. Ed.*, 2018, **57**, 11130–11139.
34 S. Ghosh, B. Dasgupta, C. Walter, P. W. Menezes and M. Driess, *Small Sci.*, 2023, **3**, 2200115.
35 S. Ghosh, B. Dasgupta, S. Kalra, M. L. P. Ashton, R. Yang, C. J. Kueppers, S. Gok, E. G. Alonso, J. Schmidt, K. Laun, I. Zebger, C. Walter, M. Driess and P. W. Menezes, *Small*, 2023, **19**, 2206679.
36 B. Chakraborty, S. Kalra, R. Beltrán-Suito, C. Das, T. Hellmann, P. W. Menezes and M. Driess, *Chem.–Asian J.*, 2020, **15**, 852–859.
37 C. Walter, S. Kalra, R. Beltrán-Suito, M. Schwarze, P. W. Menezes and M. Driess, *Mater. Today Chem.*, 2022, **24**, 100905.
38 H. Wang, M. Sun, J. Ren and Z. Yuan, *Adv. Energy Mater.*, 2023, **13**, 2203568.
39 T. Kahlstorf, J. N. Hausmann, T. Sontheimer and P. W. Menezes, *Glob. Challenges*, 2023, **7**, 1–11.
40 H. Luo, J. Barrio, N. Sunny, A. Li, L. Steier, N. Shah, I. E. L. Stephens and M. Titirici, *Adv. Energy Mater.*, 2021, **11**, 2101180.
41 J. Theerthagiri, K. Karuppasamy, J. Park, N. Rahamathulla, M. L. A. Kumari, M. K. R. Souza, E. S. F. Cardoso, A. P. Murthy, G. Maia, H.-S. Kim and M. Y. Choi, *Environ. Chem. Lett.*, 2023, **21**, 1555–1583.
42 L. Thapa, A. Bhaumik, S. Mondal and C. R. Raj, *J. Mater. Chem. A*, 2023, **11**, 26242–26251.
43 T. Begildayeva, J. Theerthagiri, S. J. Lee, A. Min, G. Kim, S. Manickam and M. Y. Choi, *Energy Environ. Mater.*, 2024, **7**, 1–9.
44 K. Xiang, D. Wu, X. Deng, M. Li, S. Chen, P. Hao, X. Guo, J. Luo and X. Fu, *Adv. Funct. Mater.*, 2020, **30**, 1–10.
45 S. Jiang, M. Wu, T. Xiao, X. Yin, Q. Gao, C. Xu, M. Zhang, H.-Q. Peng and B. Liu, *ACS Appl. Mater. Interfaces*, 2023, **15**, 55870–55876.
46 Y. Ding, Q. Xue, Q.-L. Hong, F.-M. Li, Y.-C. Jiang, S.-N. Li and Y. Chen, *ACS Appl. Mater. Interfaces*, 2021, **13**, 4026–4033.
47 V. S. Sapner, P. D. Tanwade, A. V. Munde and B. R. Sathe, *ACS Appl. Nano Mater.*, 2023, **6**, 16414–16423.
48 T.-G. Vo, P.-Y. Ho and C.-Y. Chiang, *Appl. Catal., B*, 2022, **300**, 120723.
49 X. Huang, Y. Guo, Y. Zou and J. Jiang, *Appl. Catal., B*, 2022, **309**, 121247.
50 Y. Zhu, H. Zhou, J. Dong, S.-M. Xu, M. Xu, L. Zheng, Q. Xu, L. Ma, Z. Li, M. Shao and H. Duan, *Angew. Chem., Int. Ed.*, 2023, **62**, e202219048.
51 X. Deng, G. Xu, Y. Zhang, L. Wang, J. Zhang, J. Li, X. Fu and J. Luo, *Angew. Chem., Int. Ed.*, 2021, **60**, 20535–20542.
52 C. Deng, C. Y. Toe, X. Li, J. Tan, H. Yang, Q. Hu and C. He, *Adv. Energy Mater.*, 2022, **12**, 2201047.
53 S. Ghosh, D. Bagchi, I. Mondal, T. Sontheimer, R. V. Jagadeesh and P. W. Menezes, *Adv. Energy Mater.*, 2024, **14**, 2400696.
54 S. Ghosh, J. N. Hausmann, L. Reith, G. Vijaykumar, J. Schmidt, K. Laun, S. Berendts, I. Zebger, M. Driess and P. W. Menezes, *Adv. Energy Mater.*, 2024, **14**, 2400356.

55 Y. Zhang, Z. Xue, X. Zhao, B. Zhang and T. Mu, *Green Chem.*, 2022, **24**, 1721–1731.
56 L. Huang, X. Lin, J. Zhang, C. Wang, S. Qu and Y. Wang, *J. Clean. Prod.*, 2024, **466**, 142890.
57 L. He, S. Huang, Y. Liu, M. Wang, B. Cui, S. Wu, J. Liu, Z. Zhang and M. Du, *J. Colloid Interface Sci.*, 2021, **586**, 538–550.
58 J. N. Hausmann, P. V. Menezes, G. Vijaykumar, K. Laun, T. Diemant, I. Zebger, T. Jacob, M. Driess and P. W. Menezes, *Adv. Energy Mater.*, 2022, **12**, 2202098.
59 S. Geller, *Acta Crystallogr.*, 1962, **15**, 1195–1198.
60 P. W. Menezes, C. Panda, S. Garai, C. Walter, A. Guiet and M. Driess, *Angew. Chem., Int. Ed.*, 2018, **57**, 15237–15242.
61 J. Mujtaba, L. He, H. Zhu, Z. Xiao, G. Huang, A. A. Solovev and Y. Mei, *ACS Appl. Nano Mater.*, 2021, **4**, 1776–1785.
62 H. H. Wang, J. Liu, H. H. Wang, X. Cai, X. Ye, L. Zhang, Z. Chen and Z. X. Shen, *J. Mater. Chem. A*, 2020, **8**, 14900–14907.
63 G. Greczynski and L. Hultman, *ChemPhysChem*, 2017, **18**, 1507–1512.
64 J. N. Hausmann, S. Mebs, K. Laun, I. Zebger, H. Dau, P. W. Menezes and M. Driess, *Energy Environ. Sci.*, 2020, **13**, 3607–3619.
65 J. N. Hausmann and P. W. Menezes, *Appl. Catal., B*, 2024, **342**, 123447.
66 S. Anantharaj, P. E. Karthik and S. Noda, *Angew. Chem., Int. Ed.*, 2021, **60**, 23051–23067.
67 S. Anantharaj, S. Noda, M. Driess and P. W. Menezes, *ACS Energy Lett.*, 2021, **6**, 1607–1611.
68 C. C. L. McCrory, S. Jung, I. M. Ferrer, S. M. Chatman, J. C. Peters and T. F. Jaramillo, *J. Am. Chem. Soc.*, 2015, **137**, 4347–4357.
69 J. N. Hausmann, S. Mebs, H. Dau, M. Driess and P. W. Menezes, *Adv. Mater.*, 2022, **34**, 2207494.
70 F. Dionigi, J. Zhu, Z. Zeng, T. Merzdorf, H. Sarodnik, M. Gliech, L. Pan, W.-X. Li, J. Greeley and P. Strasser, *Angew. Chem.*, 2021, **133**, 14567–14578.
71 A. S. Batchellor and S. W. Boettcher, *ACS Catal.*, 2015, **5**, 6680–6689.
72 X. Li, C. Liu, Z. Fang, L. Xu, C. Lu and W. Hou, *Small*, 2022, **18**, 1–10.
73 H. Du, T. Wang, S. He, B. Li, K. Wang, Q. Chen, Z. Du, W. Ai and W. Huang, *Adv. Funct. Mater.*, 2024, **34**, 1–11.
74 I. Mondal, P. V. Menezes, K. Laun, T. Diemant, M. Al-Shakran, I. Zebger, T. Jacob, M. Driess and P. W. Menezes, *ACS Nano*, 2023, **17**, 14043–14052.
75 A. Indra, P. W. Menezes, I. Zaharieva, H. Dau and M. Driess, *J. Mater. Chem. A*, 2020, **8**, 2637–2643.
76 Q. Wen, Y. Lin, Y. Yang, R. Gao, N. Ouyang, D. Ding, Y. Liu and T. Zhai, *ACS Nano*, 2022, **16**, 9572–9582.
77 B. Dasgupta, J. N. Hausmann, R. Beltrán-Suito, S. Kalra, K. Laun, I. Zebger, M. Driess and P. W. Menezes, *Small*, 2023, **19**, 2301258.
78 Y. Xu and B. Zhang, *ChemElectroChem*, 2019, **6**, 3214–3226.
79 H. Yang, G. Vijaykumar, Z. Chen, J. N. Hausmann, I. Mondal, S. Ghosh, V. C. J. Nicolaus, K. Laun, I. Zebger, M. Driess and P. W. Menezes, *Adv. Funct. Mater.*, 2023, **33**, 2303702.
80 R. Mariscal, P. Maireles-Torres, M. Ojeda, I. Sádaba and M. López Granados, *Energy Environ. Sci.*, 2016, **9**, 1144–1189.
81 H. Yang, P. V. Menezes, G. Dai, G. Vijaykumar, Z. Chen, M. Al-Shakran, T. Jacob, M. Driess and P. W. Menezes, *Appl. Catal., B*, 2023, **324**, 122249.